INTERNATIONAL JOURNAL FOR NUMERICAL METHODS IN ENGINEERING
Int. J. Numer. Meth. Engng. **45**, 1139–1164 (1999)

THE SPECTRAL ELEMENT METHOD FOR ELASTIC WAVE EQUATIONS—APPLICATION TO 2-D AND 3-D SEISMIC PROBLEMS

DIMITRI KOMATITSCH[1], JEAN-PIERRE VILOTTE[1,*], ROSSANA VAI[2],
JOSÉ M. CASTILLO-COVARRUBIAS[2] AND FRANCISCO J. SÁNCHEZ-SESMA[2]

[1]*Département de Sismologie (URA 195) and Département de Modélisation Physique et Numérique,*
Institut de Physique du Globe de Paris, 4 Place Jussieu, 75252 – Paris Cedex 05, France
[2]*Instituto de Ingeniería, UNAM, Cd. Universitaria, Apdo 70-412, Coyoacán 04510, México D.F., Mexico*

SUMMARY

A spectral element method for the approximate solution of linear elastodynamic equations, set in a weak form, is shown to provide an efficient tool for simulating elastic wave propagation in realistic geological structures in two- and three-dimensional geometries. The computational domain is discretized into quadrangles, or hexahedra, defined with respect to a reference unit domain by an invertible local mapping. Inside each reference element, the numerical integration is based on the tensor-product of a Gauss–Lobatto–Legendre 1-D quadrature and the solution is expanded onto a discrete polynomial basis using Lagrange interpolants. As a result, the mass matrix is always diagonal, which drastically reduces the computational cost and allows an efficient parallel implementation. Absorbing boundary conditions are introduced in variational form to simulate unbounded physical domains. The time discretization is based on an energy-momentum conserving scheme that can be put into a classical explicit-implicit predictor/multicorrector format. Long term energy conservation and stability properties are illustrated as well as the efficiency of the absorbing conditions. The accuracy of the method is shown by comparing the spectral element results to numerical solutions of some classical two-dimensional problems obtained by other methods. The potentiality of the method is then illustrated by studying a simple three-dimensional model. Very accurate modelling of Rayleigh wave propagation and surface diffraction is obtained at a low computational cost. The method is shown to provide an efficient tool to study the diffraction of elastic waves and the large amplification of ground motion caused by three-dimensional surface topographies. Copyright © 1999 John Wiley & Sons, Ltd.

KEY WORDS: elastodynamics; explicit spectral element method; seismology

INTRODUCTION

In computational seismology and earthquake engineering, considerable efforts have been devoted for developing highly accurate numerical techniques for the solution of elastic wave equations. An increasing number of applications, such as elastic waveform modelling for realistic geological media or the assessment of site effects in earthquake ground motion, have underlined the need for

---

[*] Correspondence to: Jean-Pierre Vilotte, Département de Sismologie, Institut de Physique du Globe de Paris, 4 Place Jussieu, 75252 Paris Cedex 05, France. E-mail: vilotte@ipgp.jussieu.fr

Contract/grant sponsor: DGAPA-UNAM; Contract/grant number: IN 108295

CCC 0029–5981/99/211139–26$17.50

Received 11 March 1998
Revised 5 October 1998

high-performance methods that are able to routinely handle complex two- and three-dimensional geological configurations of high practical interest.

Finite difference methods, that have been widely used in computational seismology, require a large number of grid points to achieve the expected accuracy [1, 2], even with high-order explicit or implicit spatial operators [3, 4]. Free surface boundaries and complex configurations coarse modelling produce lack of precision in the simulation of Rayleigh wave propagation [5, 6]. In practice, a difficult trade-off between numerical dispersion and computational cost is required [7, 8].

Finite element methods have attracted somewhat less interest among seismologists [9]. One of the reasons for that is that low-order finite element methods exhibit poor dispersion properties [10], while higher-order classical finite elements raise some troublesome problems like the occurrence of spurious waves. Recently, space–time and Galerkin/least-squares finite element methods, related to Hamilton's principle, have been introduced both for acoustic and full elastic wave propagation [11–13] with some success, even though application of these methods to realistic seismological problems have still to be shown.

Boundary element methods [14, 15] have been successfully applied in seismology [16, 17]. The main advantages are that the solution is sought over a domain one dimension lower than the physical domain, and that the radiation condition is *a priori* satisfied. Such methods require homogeneous domains and linear constitutive laws (unless a scheme in time domain is adopted). The linear system to be solved is non-symmetric and, in some cases, it can be ill-conditioned. The expected computational advantage in processing time and storage requirement is, therefore, not always achieved.

In their pioneering work [18], Aki and Larner represented complex wavefields by a simple superposition of plane waves. Since then, this technique (the discrete wave number method, DWN) has been extended by many authors [19, 20]. Particularly interesting has been the combination of discrete wave number expansion for Green function [19, 21] with a boundary integral representation [22].

Higher-order methods like spectral methods, that enable to achieve the expected accuracy using few grid points per wavelength, have also been proposed for elastodynamics problems [23, 24]. To deal with more general boundary conditions, the set of truncated Fourier series is usually replaced by a set of algebraic polynomials (Chebyschev or Legendre) in space [25, 26]. In these methods, the accuracy is shown to depend strongly on the choice of the collocation points. A limitation of the approach is that the non-uniform spacing of the algebraic polynomial collocation points puts stringent constraints on the time-step [27]. Also, spectral methods, like finite difference methods, cannot handle complex geometries easily nor, if based on a strong formulation, realistic free surfaces. To overcome these drawbacks, several approaches have been considered like, for instance, the use of curvilinear co-ordinate systems [25, 27], or domain decomposition methods [28], but with an increase of the computational cost.

Understanding of the similarity between collocation methods and variational formulations with consistent quadrature lead, in fluid dynamics, to the spectral element method [29, 30] which may be related to the h–p version of the finite element method [31]. This approach, which brings new flexibility to treat complex geometries, has been proposed for wave propagation problems recently [32–34].

This paper describes a practical spectral element method to solve problems of two- and three-dimensional elastic wave propagation in complex geometries. The method, which stems from a weak variational formulation, allows a flexible treatment of boundaries or interfaces and deals with free-surface boundary conditions naturally. It combines the geometrical flexibility of a low-order method with the exponential convergence rate associated with spectral techniques, and suffers from minimal numerical dispersion and diffusion. The unbounded domain is simulated by introducing artificial boundaries on which absorbing conditions are enforced. As far as the spatial discretization is concerned, our formulation is based on Legendre polynomials and Gauss–Lobatto–Legendre quadrature, which leads to fully explicit schemes while retaining the efficient sum-factorization techniques [35]. Although the particular choice of the sets of algebraic polynomials, Chebyshev or Legendre, and collocation points, related to the numerical quadrature, does not generally affect the error estimate significantly, it greatly affects the conditioning and sparsity of the resulting set of algebraic equations and it is critical for the efficiency of parallel implementations [36]. Our time discretization makes use of an energy-momentum conserving scheme, that can be rewritten into a classical explicit–implicit predictor/multicorrector format that allows an efficient parallel implementation as well.

The accuracy of the method is first illustrated by showing energy conservation or dissipation, depending on the boundary conditions, in a simple rectangular domain. Then the results for the incidence of a surface Rayleigh wave upon a semicircular canyon are compared with those obtained by Kawase [37] using the discrete wavenumber-boundary element method. These reference results have been extensively verified and are trustworthy. The agreement is very good. In order to illustrate the capabilities of the method, simulations of some other two- and three-dimensional problems are presented. The results obtained for a two-dimensional layered medium, excited by an explosive linear source, are compared with synthetic seismograms calculated using the indirect boundary element method (IBEM) [38, 39]. Again the agreement is very good. Finally, a three-dimensional topography is studied. The possibilities of the method are explored for simple yet rather realistic configurations.

ELASTIC WAVE EQUATIONS

We consider an elastic inhomogeneous medium occupying an open, bounded region $\bar{\mathbf{\Omega}} \subset \mathbb{R}^{n_d}$, where n_d is the number of space dimensions. The displacement and velocity vectors at a point $\mathbf{x}$ and time t are denoted by $\mathbf{u}(\mathbf{x},t)$ and $\mathbf{v}(\mathbf{x},t)$, respectively, where $\mathbf{x} \in \bar{\mathbf{\Omega}}$ and $t \in \mathbf{I} = [0,T]$, with $\mathbf{I}$ the time interval of interest. The equations of the initial/boundary-value problem of elastic wave propagation are

$$\rho\dot{\mathbf{v}} = \mathrm{div}[\boldsymbol{\sigma}] + \mathbf{f} \tag{1}$$

$$\rho\dot{\mathbf{u}} = \rho\mathbf{v} \tag{2}$$

with the initial conditions

$$\mathbf{u}(\mathbf{x},0) = \mathbf{u}_0(\mathbf{x}) \tag{3}$$

$$\mathbf{v}(\mathbf{x},0) = \mathbf{v}_0(\mathbf{x}) \tag{4}$$

where $\boldsymbol{\sigma}(\mathbf{x},t)$ is the stress tensor; $\mathbf{f}(\mathbf{x},t)$ is a generalized body force; $\rho = \rho(\mathbf{x}) > 0$ is the mass density; $\mathbf{u}_0(\mathbf{x})$ and $\mathbf{v}_0(\mathbf{x})$ are, respectively, the initial displacement and velocity fields. A dot over a symbol indicates partial differentiation with respect to time. In component forms, $\mathrm{div}[\boldsymbol{\sigma}]$ is $\sigma_{ij,j}$ with $i,j = 1,2,\ldots,n_d$. The stress is determined by Hooke's law

$$\boldsymbol{\sigma}(\nabla\mathbf{u}) = \mathbf{c}(\mathbf{x}) : \nabla\mathbf{u}(\mathbf{x},t) \tag{5}$$

where $\mathbf{c}(\mathbf{x})$ is the elastic tensor at a point $\mathbf{x}$ and $\nabla\mathbf{u} = u_{i,j}$ is the displacement gradient. In components form,

$$\sigma_{ij}(\mathbf{x}, t) = c_{ijkl}(\mathbf{x}) u_{k,l}(\mathbf{x}, t) \tag{6}$$

with $u_{k,l} = \partial u_k / \partial x_l$. Since we are considering an elastic medium, $\mathbf{c}(\mathbf{x})$ is symmetric

$$c_{ijkl} = c_{jikl} = c_{ijlk} = c_{klij} \tag{7}$$

and positive definite

$$c_{ijkl}\psi_{ij}\psi_{kl} > 0 \quad \forall \psi_{ij} = \psi_{ji} \neq 0 \tag{8}$$

In computational seismology, two simple source terms are often considered. The first is a point force

$$\mathbf{f}(\mathbf{x}, t) = f_i \hat{\mathbf{e}}_i \delta(\mathbf{x} - \mathbf{x_0}) \mathscr{G}(t - t_0) \tag{9}$$

where f_i is the magnitude of the force applied at point $\mathbf{x_0}$ and at time t_0 in the $\hat{\mathbf{e}}_i$ direction; $\delta(\mathbf{x} - \mathbf{x_0})$ is the Dirac function and $\mathscr{G}(t - t_0)$ is an arbitrary function describing the force time variation. The second is an equivalent body force, derived from a seismic moment density tensor distribution, which represents the equivalent stress distribution associated with seismic sources

$$\mathbf{f}(\mathbf{x}, t) = -\operatorname{div}[\mathbf{m}(\mathbf{x}, t)] \tag{10}$$

where $\mathbf{m}(\mathbf{x}, t)$ is the seismic moment density tensor at point $\mathbf{x}$ and time t. In many seismological applications, a point source approximation to a seismic event may be quite satisfactory and finite sources may be generated by straightforward superposition of simple point sources [40]. For such a case we have

$$\mathbf{m}(\mathbf{x}, \mathbf{t}) = \mathbf{M}(t) \delta(\mathbf{x} - \mathbf{x_0}) \tag{11}$$

where $\mathbf{M}$ is a symmetric tensor that has all the properties of a stress tensor. The spherical part of the moment tensor carries information about P waves only, while the deviatoric part propagates S and P waves. In three dimensions, depending on the eigenvalues λ_j of $\mathbf{M}$, pure shear faults ($\lambda_1 = -\lambda_3; \lambda_2 = 0$), pure tension cracks ($\lambda_1 \neq 0; \lambda_2 = \lambda_3 = 0$), explosive sources ($\lambda_1 = \lambda_2 = \lambda_3 \neq 0$) or compensated linear dipoles ($\lambda_1 \neq 0; \lambda_2 = \lambda_3 = -\lambda_1/2$) can be simulated. Body wave radiation depends linearly on the rate of change of the moment tensor. A simple rise time approximation can be used:

$$\mathbf{M}(t) = \mathbf{M}_0 \mathscr{G}(t - t_0) \tag{12}$$

where $\mathbf{M}_0$ is a constant moment tensor. Our formulation provides a natural way to introduce these point sources. Also, for elastic, isotropic media we can completely describe the incidence of plane waves using analytical means and give tractions at a boundary to enforce their cancellation. Alternatively, from the analytical solution it is also possible to compute the initial displacement, velocity and acceleration for all the points of the model.

Boundary conditions

In geophysical problems, solutions are often assumed to extend to infinity along some directions. As a result, a fundamental obstacle to the direct application of several numerical methods is the presence of an unbounded domain. When the numerical method does not *a priori* satisfy the radiation condition, the formulation has to be defined over a bounded region by introducing an artificial external boundary with appropriate absorbing boundary conditions. The boundary of the open domain $\mathbf{\Omega}$, denoted by $\mathbf{\Gamma}$, is therefore decomposed into

$$\mathbf{\Gamma} = \mathbf{\Gamma}^{\text{int}} \cup \mathbf{\Gamma}^{\text{ext}} \tag{13}$$

where $\mathbf{\Gamma}^{\text{int}}$ and $\mathbf{\Gamma}^{\text{ext}}$ denote non-overlapping subregions, $\mathbf{\Gamma}^{\text{ext}}$ being the artificial external boundary and $\mathbf{\Gamma}^{\text{int}}$ the physical boundary.

Physical boundary conditions. The physical boundary $\mathbf{\Gamma}^{\text{int}}$ is divided into two non-overlapping parts $\mathbf{\Gamma}_T^{\text{int}}$ and $\mathbf{\Gamma}_{\mathbf{g}}^{\text{int}}$, where the traction vector and the displacement field are respectively prescribed:

$$\boldsymbol{\sigma}(\mathbf{x}, t) \cdot \mathbf{n}(\mathbf{x}) = \mathbf{T}(\mathbf{x}, t) \quad \text{on } \mathbf{\Gamma}_T^{\text{int}} \tag{14}$$

$$\mathbf{u}(\mathbf{x}, t) = \mathbf{g}(\mathbf{x}, t) \quad \text{on } \mathbf{\Gamma}_{\mathbf{g}}^{\text{int}} \tag{15}$$

$\mathbf{T}(\mathbf{x}, t)$ is the prescribed boundary traction vector at a point $\mathbf{x}$ and time t and $\mathbf{g}(\mathbf{x}, t)$ the prescribed displacement field. In component form $\boldsymbol{\sigma} \cdot \mathbf{n}$ is $\sigma_{ij} n_j$.

Absorbing boundary conditions. The representation of the radiation condition associated with the external boundary is a difficult problem, and numerous approximate schemes have been proposed in the geophysical literature [41]. Employing an asymptotic expansion of the far-field solution to generate a sequence of local boundary operators [42], exact non-local boundary conditions have now been derived. They are, however, computationally expensive and their application has been mainly restricted up to now to accoustic problems [43, 44]. We assume here a simple local approximation based on the variational formulation of the paraxial condition originally introduced by Clayton and Engquist [45]. Along the boundary surface, the local transient impedance of $\mathbf{\Gamma}^{\text{ext}}$ is approximated by use of a limited wave-number expansion of the elastodynamics equation in the Fourier domain. Such an approximation is accurate for waves impinging on the boundary at small angles only. In the following, a first-order approximation, close to that of Stacey [46], is retained. On the artificial external boundary, the condition is expressed as

$$\mathbf{t} = \mathrm{c}_{\mathrm{L}} \rho [\mathbf{v} \cdot \mathbf{n}] \mathbf{n} + c_{\mathrm{T}} \rho \mathbf{v}_{\mathrm{T}} \tag{16}$$

where $\mathbf{t}$ is the boundary traction; $\mathbf{n}$ is the unit outward normal to the surface; $\mathbf{v}_{\mathrm{T}} = \mathbf{v} - [\mathbf{v} \cdot \mathbf{n}]\mathbf{n}$ the projection of the velocity field on the surface; c_L and c_{T} are the propagation velocities of P (longitudinal) and S (transversal) waves, respectively.

Variational formulation

In order to outline the spectral element method, we first start with the variational formulation of the physical problem. The solution $\mathbf{u}$ is searched in the space of kinematically admissible displacements:

$$\mathscr{S}_t = \{\mathbf{u}(\mathbf{x}, t) \in H^1(\mathbf{\Omega})^{n_d} : \mathbf{\Omega} \times \mathbf{I} \rightarrow \mathbb{R}^{n_d}; \mathbf{u}(\mathbf{x}, t) = \mathbf{g}(\mathbf{x}, t) \text{ on } \mathbf{\Gamma}_g^{\text{int}} \times \mathbf{I}\} \tag{17}$$

where H^1 is the classical Sobolev space that denotes the space of square-integrable functions with square-integrable generalized first derivatives. Introducing the function space $\mathscr{V}$ of the test-functions $\mathbf{w}$:

$$\mathscr{V} = \{\mathbf{w}(\mathbf{x}) \in H^1(\boldsymbol{\Omega})^{n_d} : \boldsymbol{\Omega} \rightarrow \mathbb{R}^{n_d}; \mathbf{w}(\mathbf{x}) = 0 \text{ on } \boldsymbol{\Gamma}_g^{\text{int}}\} \tag{18}$$

the weak form of the problem (1)–(3) reads: find $\mathbf{u} \in \mathscr{S}_t$, such that $\forall t \in \mathbf{I}$ and $\forall \mathbf{w} \in \mathscr{V}$

$$(\mathbf{w}, \rho\dot{\mathbf{v}}) + a(\mathbf{w}, \mathbf{u}) = (\mathbf{w}, \mathbf{f}) + \langle \mathbf{w}, \mathbf{T} \rangle_{\boldsymbol{\Gamma}_T^{\text{int}}} + \langle \mathbf{w}, \mathbf{t} \rangle_{\boldsymbol{\Gamma}^{\text{ext}}} \tag{19}$$

$$(\mathbf{w}, \rho\dot{\mathbf{u}}) = (\mathbf{w}, \rho\mathbf{v}) \tag{20}$$

with

$$(\mathbf{w}, \rho\mathbf{u}(.,t)|_{t=0}) = (\mathbf{w}, \rho\mathbf{u}_0) \tag{21}$$

$$(\mathbf{w}, \rho\mathbf{v}(.,t)|_{t=0}) = (\mathbf{w}, \rho\mathbf{v}_0) \tag{22}$$

where $(\cdot,\cdot)$ is the classical L^2 inner product, and

$$(\mathbf{w}, \mathbf{u}) = \int_{\boldsymbol{\Omega}} \mathbf{v} \cdot \mathbf{u} \, \mathrm{d}V \tag{23}$$

$$\langle \mathbf{w}, \mathbf{u} \rangle_{\boldsymbol{\Gamma}} = \int_{\boldsymbol{\Gamma}} \mathbf{w} \cdot \mathbf{u} \, \mathrm{d}\Gamma \tag{24}$$

The H^1 bilinear form $a(\cdot,\cdot)$ is the strain-energy inner product and is symmetric, V-elliptic and continuous:

$$a(\mathbf{w}, \mathbf{u}) = \int_{\boldsymbol{\Omega}} \boldsymbol{\sigma} : \nabla\mathbf{w} \, \mathrm{d}V = \int_{\boldsymbol{\Omega}} \nabla\mathbf{w} : \mathbf{c} : \nabla\mathbf{u} \, \mathrm{d}V \tag{25}$$

where in component form, $\sigma : \nabla\mathbf{w} = \sigma_{ij} \partial w_i / \partial x_j$.

Spatial discretization

The original physical domain $\bar{\boldsymbol{\Omega}}$ is discretized into n_{el} non-overlapping elementary quadrilaterals $\bar{\boldsymbol{\Omega}}_e$. This partition $\bar{\boldsymbol{\Omega}} = \bigcup_{e=1}^{n_{\text{el}}} \bar{\boldsymbol{\Omega}}_e$ of the domain is generically referred to as the quadrangulation and is denoted $\mathscr{Q}^h$. The restriction of the test-function $\mathbf{w}$ to the element $\bar{\boldsymbol{\Omega}}_e$ is denoted $\mathbf{w}^h|_{\bar{\boldsymbol{\Omega}}_e}$. Let us denote $\Lambda = [-1, 1]$, and $\square$ the reference volume Λ^{n_d}, which is a square or a cube depending on the spatial dimension n_d of the problem. For each element $\bar{\boldsymbol{\Omega}}_e \in \mathscr{Q}^h$, we suppose that there exists an invertible mapping function $\mathscr{F}_e$ between the reference volume $\square$ and a local coordinate system $\boldsymbol{\xi}$ of the element $\bar{\boldsymbol{\Omega}}_e$, defined as $\mathscr{F}_e : \square \rightarrow \bar{\boldsymbol{\Omega}}_e$ such that $\mathbf{x}(\boldsymbol{\xi}) = \mathscr{F}_e(\boldsymbol{\xi})$. We can then make use of this mapping to go between the physical and the reference domain, and vice versa. Associated with the spatial discretization $\mathscr{Q}^h$, one introduces a piecewise-polynomial approximation $\mathscr{S}_N^h \times \mathscr{V}_N^h$ of the functional space $\mathscr{S} \times \mathscr{V}$ defined previously:

$$\mathscr{S}_N^h = \{\mathbf{u}^h \in \mathscr{S} \colon \mathbf{u}^h \in L^2(\boldsymbol{\Omega})^{n_d} \text{ and } \mathbf{u}^h|_{\bar{\boldsymbol{\Omega}}_e} \circ \mathscr{F}_e \in [\mathbb{P}_N(\square)]^{n_d}\} \tag{26}$$

and

$$\mathscr{V}_N^h = \{\mathbf{w}^h \in \mathscr{V} \colon \mathbf{w}^h \in L^2(\boldsymbol{\Omega})^{n_d} \text{ and } \mathbf{w}^h|_{\bar{\boldsymbol{\Omega}}_e} \circ \mathscr{F}_e \in [\mathbb{P}_N(\square)]^{n_d}\} \tag{27}$$

Since $\mathscr{V}_N^h \subset \mathscr{V}$, given two adjacent elements, say $\mathbf{\Omega}_{e1}$ and $\mathbf{\Omega}_{e2}$, and any $\mathbf{w}^h \in \mathscr{V}_N^h$, the restrictions of $\mathbf{w}^h$ to these elements must coincide along the intersection of their respective boundaries. The mappings $\mathscr{F}_{e_1}$ and $\mathscr{F}_{e_2}$ should be compatible in the sense that if

$$\bar{\mathbf{\Omega}}_{e1} \cap \bar{\mathbf{\Omega}}_{e2} = \mathscr{F}_{e_1}(\gamma_1) = \mathscr{F}_{e_2}(\gamma_2) \tag{28}$$

γ_1 and γ_2 being two edges of the reference square, then $\mathscr{F}_{e_2}^{-1} \circ \mathscr{F}_{e_1}$ must be an affine mapping from γ_1 onto γ_2. In particular, the set of nodes located on $\bar{\mathbf{\Omega}}_{e1} \cap \bar{\mathbf{\Omega}}_{e2}$, generated as the images by $\mathscr{F}_{e_1}$ of the Gauss–Lobatto nodes on γ_1 must coincide with those that are images of the Gauss–Lobatto nodes on γ_2. This ensures the continuity across element boundaries.

Inside each reference volume $\square$, $[\mathbb{P}_N(\square)]^{n_d}$ is taken to be the space generated as the tensor-product space of all polynomials of degree $\leqslant N$ in each of the n_d spatial directions. The characteristic length scale associated with the underlying mesh is denoted h. The spectral element spatial discretization can hence be characterized by the total number of elements n_{el} and by the polynomial degree N used on each element. The discrete variational problem then reads: find $\mathbf{u}_N^h \in \mathscr{S}_{N,t}^h$, such that $\forall t \in \mathbf{I}$ and $\forall \mathbf{w}_N^h \in \mathscr{V}_N^h$,

$$(\mathbf{w}_N^h, \rho\dot{\mathbf{v}}_N^h) + a(\mathbf{w}_N^h \mathbf{u}_N^h) = (\mathbf{w}_N^h, \mathbf{f}) + \langle \mathbf{w}_N^h, \mathbf{T} \rangle_{\mathbf{\Gamma}_T^{\text{int}}} + \langle \mathbf{w}_N^h, \mathbf{t} \rangle_{\mathbf{\Gamma}^{\text{ext}}} \tag{29}$$

$$(\mathbf{w}_N^h, \rho\dot{\mathbf{u}}_N^h) = (\mathbf{w}_N^h, \rho\mathbf{v}_N^h) \tag{30}$$

with

$$(\mathbf{w}_N^h, \rho\mathbf{u}_N^h(.,t)|_{t=0}) = (\mathbf{w}_N^h, \rho\mathbf{u}_{0N}^h) \tag{31}$$

$$(\mathbf{w}_N^h, \rho\mathbf{v}_N^h(.,t)|_{t=0}) = (\mathbf{w}_N^h, \rho\mathbf{v}_{0N}^h) \tag{32}$$

The spatial discretization must be completed by defining the discrete inner products associated with the continuous inner products involved in the variational formulation. This is done by choosing a numerical quadrature for integrating each element integral, defined over the elementary domain $\bar{\mathbf{\Omega}}_e$ in the $\mathbf{x}$-space, after a pull back on the parent domain $\square$, using the local mapping $\mathscr{F}_e$. Although the particular choice of the unisolvent basis points ξ^i on the reference element and the numerical quadrature can be made independently, in order to take advantage of efficient sum-factorization techniques, and to improve the conditioning and sparsity of the resulting set of algebraic equations, the unisolvent set of $(N+1)^{n_d}$ basis points for $\mathbb{P}_N$ is taken to be the n_d tensor product of the $N+1$ Gauss–Lobatto–Legendre points. For $n_d = 3$, this defines the grid $\Xi_N^e = \{(\xi^i, \eta^j, \zeta^k);\ i,j,k = 1,\ldots,N+1\}$, with ξ^i, η^j and ζ^k the Gauss–Lobatto points in each direction of the reference element $\square$. The discrete inner products are therefore based on the tensor-product of 1-D Gauss–Lobatto–Legendre formulas. The quadrature points are the same as the basis points, and for $N+1$ quadrature points, all polynomials of degree $\leqslant 2N-1$ can be integrated exactly. The variational formulation requires two inner products, the L^2 inner product and the H^1 bilinear form, their discrete formulation being, for $n_d = 3$:

$$(\mathbf{w}_N^h, \mathbf{u}_N^h)_N = \sum_{e=1}^{n_{\text{el}}} \sum_{i,j,k=1}^{N+1} \mathbf{w}_N^h|_{\bar{\mathbf{\Omega}}_e}(\xi^i, \eta^j, \zeta^k)\mathbf{u}_N^h|_{\bar{\mathbf{\Omega}}_e}(\xi^i, \eta^j, \zeta^k)|J_e(\xi^i, \eta^j, \zeta^k)|\omega_{ijk} \tag{33}$$

$$a_N(\mathbf{w}_N^h,\mathbf{u}_N^h)=\sum_{e=1}^{n_{\mathrm{el}}}\sum_{i,j,k=1}^{N+1}\boldsymbol{\sigma}(\xi^i,\eta^j,\zeta^k):\tilde{\nabla}\mathbf{w}_N^h|_{\bar{\boldsymbol{\Omega}}_e}(\xi^i,\eta^j,\zeta^k)|J_e(\xi^i,\eta^j,\zeta^k)|\omega_{ijk} \tag{34}$$

$$=\sum_{e=1}^{n_{\mathrm{el}}}\sum_{i,j,k=1}^{N+1}\tilde{\nabla}\mathbf{w}_N^h|_{\bar{\boldsymbol{\Omega}}_e}(\xi^i,\eta^j,\zeta^k):\mathbf{c}(\xi^i,\eta^j,\zeta^k):\tilde{\nabla}\mathbf{u}_N^h|_{\bar{\boldsymbol{\Omega}}_e}(\xi^i,\eta^j,\zeta^k)|J_e(\xi^i,\eta^j,\zeta_k)|\omega_{ijk} \tag{35}$$

where J_e is the Jacobian of the co-ordinate transformation at the element level, $\omega_{ijk}=\omega_i\omega_j\omega_k$ with $\omega_i>0$ are the quadrature weights of the 1D Gauss–Lobatto–Legendre rule, and $\tilde{\nabla}$ is the pull back of the gradient operator on the reference volume $\square$:

$$\nabla_{\mathbf{x}}\mathbf{w}_N^h|_{\bar{\boldsymbol{\Omega}}_e}=\tilde{\nabla}\mathbf{w}_N^h|_{\bar{\boldsymbol{\Omega}}_e}(\boldsymbol{\xi})=\nabla_{\boldsymbol{\xi}}\mathbf{w}_N^h|_{\bar{\boldsymbol{\Omega}}_e}(\boldsymbol{\xi})\mathbf{F}_e^{-1}(\boldsymbol{\xi}) \tag{36}$$

$\mathbf{F}_e(\boldsymbol{\xi})=\partial_{\boldsymbol{\xi}}\mathscr{F}_e(\boldsymbol{\xi})$ being the gradient of the geometrical transformation, and $\boldsymbol{\xi}=(\xi,\eta,\zeta)$. Such a consistent integration is shown to be sufficient for complex geometries or heterogeneous elastic parameters [47], which is an important consideration when wave equations are to be solved for situations of practical interest.

The piecewise polynomial approximation $\mathbf{w}_N^h$ of $\mathbf{w}$ is defined using the Lagrange interpolation operator $\mathscr{I}_N$ on the Gauss–Lobatto–Legendre grid Ξ_N^e : $\mathscr{I}_N(\mathbf{w}|_{\bar{\boldsymbol{\Omega}}_e})$ is the unique polynomial of $\mathbb{P}_N(\square)$ which coincides with $\mathbf{w}|_{\bar{\boldsymbol{\Omega}}_e}$ at the $(N+1)^{n_d}$ points of Ξ_N^e. The corresponding Lagrange interpolants Q_N^e are therefore the tensor-product of n_d one-dimensional Lagrange interpolants of degree N. For $n_d=3$, $Q_N^{ijk,e}\in[\mathbb{P}_N(\square)]^3$,

$$Q_N^{ijk,e}(\xi^l,\eta^m,\zeta^n)=\delta_{il}\delta_{jm}\delta_{kn}\quad\forall(\xi^l,\eta^m,\zeta^n)\in\Xi_N^e \tag{37}$$

$$\mathbf{w}_N^h|_{\bar{\boldsymbol{\Omega}}_e}(x,y,z)=\mathscr{I}_N(\mathbf{w}|_{\bar{\boldsymbol{\Omega}}_e})=\sum_{i,j,k=1}^{N+1}Q_N^{ijk,e}(\xi^i,\eta^j,\zeta^k)\mathbf{w}_{ijk}^e \tag{38}$$

with

$$Q_N^{ijk,e}(\xi,\eta,\zeta)=l_N^{i,e}(\xi)\otimes l_N^{j,e}(\eta)\otimes l_N^{k,e}(\zeta) \tag{39}$$

where $l_N^{i,e}(\xi)$ denotes the characteristic 1-D Lagrange polynomial of degree N associated with the Gauss–Lobatto–Legendre point i of the corresponding one dimensional quadrature formula; $\mathbf{x}=\mathscr{F}_e(\boldsymbol{\xi})$ and $\mathbf{w}_{ijk}^e=\mathbf{w}_N^h|_{\bar{\boldsymbol{\Omega}}_e}\circ\mathscr{F}_e(\xi^i,\eta^j,\zeta^k)$, and $\delta_{il}=1$ if $i=l$, $\delta_{il}=0$ otherwise.

The procedure outlined above leads, like in classical finite element methods, to a coupled system of second-order ordinary differential equations in time:

$$\mathscr{M}\dot{\mathbf{v}}(t)=\mathscr{F}^{\mathrm{ext}}(t)-\mathscr{F}^{\mathrm{int}}(\mathbf{u}_N^h,t),\quad\dot{\mathbf{u}}(t)=\mathbf{v}(t) \tag{40}$$

where now $\mathbf{u}(t)=\{\mathbf{u}_{ijk}(t)\}$ and $\mathbf{v}(t)=\{\mathbf{v}_{ijk}(t)\}$ respectively denote the displacement and velocity vectors of $n_d\times n_{\mathrm{node}}$ components, n_{node} being the total number of integration points that form the global integration grid Ξ_N defined as the assembly of the elementary integration grids on each element $\Xi_N=\bigcup_e\Xi_N^e$.

The internal force vector $\mathscr{F}^{\mathrm{int}}$, at node $\{lmn\}$, is defined as

$$\mathscr{F}_{lmn}^{\mathrm{int}}=a_N(Q_N^{lmn},\mathbf{u}_N^h)-\langle Q_N^{lmn},\mathbf{t}(\mathbf{u}_N^h)\rangle_{N,\Gamma_{\mathrm{ext}}} \tag{41}$$

where the element summation in the second term on the right-hand side extends to all the elements that share a face with the artificial external boundary Γ_{ext}. The external force vector $\mathscr{F}^{\text{ext}}$ at node $\{lmn\}$ is

$$\mathscr{F}^{lmn,\text{ext}} = (Q_N^{lmn}, \mathbf{f})_N + \langle Q_N^{lmn}, \mathbf{T}\rangle_{N,\Gamma_{\text{T}}^{\text{int}}} \tag{42}$$

When considering an equivalent body force derived from a seismic moment tensor density distribution with a localized spatial support—see equation (10)—the term on the right-hand side in equation (42) can be written after integration by parts:

$$\mathscr{F}^{lmn,\text{ext}} = \sum_e \left[\int_{\mathbf{\Omega}_e} \nabla Q_N^{lmn,e} : \mathbf{m}(\mathbf{x},t)\, \mathrm{d}V \right] + \langle Q_N^{lmn}, \mathbf{T}\rangle_{N,\Gamma_{\text{T}}^{\text{int}}} \tag{43}$$

where the assembly operation involves only the elements that belong to the spatial support of the moment density distribution for the first term and elements that share a common face with the physical boundary $\Gamma_{\text{T}}^{\text{int}}$ for the second term. The mass matrix $\mathscr{M}$ is simply defined as

$$\mathscr{M} = \sum_{e=1}^{n_{\text{el}}} \int_{\mathbf{\Omega} e} Q_N^e \otimes Q_N^e \rho \, \mathrm{d}V \tag{44}$$

An attractive property of the method is that, in contrast with classical finite element methods, due to the consistent integration scheme and the use of Gauss–Lobatto Legendre formulas, the mass matrix $\mathscr{M}$ is by construction always diagonal, leading to a fully explicit scheme. This was first pointed by Maday and Patera in the context of spectral approximation of elliptic and Navier–Stokes equations [30]. The spectral element method therefore combines the geometrical flexibility of the finite element method with the fast convergence associated with spectral techniques. The discrete solution suffers from minimal numerical dispersion and diffusion, a fact of primary importance in the solution of realistic geophysical problems [44, 48].

Discretization in time

We discretize the time interval of interest using a time step Δt. Introducing three control parameters α, β and γ, all belonging to $[0,1]$, the semi-discrete momentum equation is then enforced in conservative form [49] at $t_{n+\alpha}$:

$$\frac{1}{\Delta t}\mathscr{M}[\mathbf{v}_{n+1} - \mathbf{v}_n] = \mathscr{F}^{\text{ext}}_{n+\alpha} - \mathscr{F}^{\text{int}}(\mathbf{u}^h_{n+\alpha}, \mathbf{v}^h_{n+\alpha}) \tag{45}$$

$$\mathbf{u}_{n+1} = \mathbf{u}_n + \Delta t \left[\left(1 - \frac{\beta}{\gamma}\right)\mathbf{v}_n + \frac{\beta}{\gamma}\mathbf{v}_{n+1} \right] + \Delta t^2 \left(\frac{1}{2} - \frac{\beta}{\gamma} \right) \mathbf{a}_n \tag{46}$$

$$\mathbf{a}_{n+1} = \frac{1}{\gamma \Delta t}[\mathbf{v}_{n+1} - \mathbf{v}_n] + \left(1 - \frac{1}{\gamma}\right)\mathbf{a}_n \tag{47}$$

where $\mathbf{u}_{n+\alpha} \doteq \alpha \mathbf{u}_{n+1} + (1-\alpha)\mathbf{u}_n$ and $\mathbf{F}^{\text{ext}}_{n+\alpha} \doteq \alpha \mathscr{F}^{\text{ext}}_{n+1} + (1-\alpha)\mathscr{F}^{\text{ext}}_n$. Simo *et al.* [49] have shown that for $\alpha = \beta/\gamma = 1/2$ this energy–momentum method exactly preserves the total energy, linear and angular momenta (these values define an acceleration-independent algorithm). It is second-order accurate if and only if $\alpha = 1/2$. This Newmark-type scheme can be generalized to a predictor-multicorrector format that allows an efficient parallelization. The scheme is shown in this case to be conditionally stable, and the associated Courant condition depends on the size of the smallest grid cell. Denoting n_{el} the total number of elements and n_d the spatial dimension, the average size of a spectral element for a fixed size of the model under study is proportional to ${n_{\mathrm{el}}}^{-1/n_d}$. It can also be shown that on the reference interval $[-1, 1]$, denoting N the polynomial order, the minimum grid spacing between two Gauss–Lobatto–Legendre points occurs at the edges of the interval, both in -1 and in 1, and is proportional to N^{-2}. Therefore, the Courant condition, related to the size of the smallest grid cell, can be written $\Delta t_{\mathrm{C}} < \mathcal{O}({n_{\mathrm{el}}}^{-1/n_d} N^{-2})$. One can note that with the help of a sub-stepping procedure [50], the scheme can achieve fourth-order accuracy, with no additional storage or extra computations of high-order gradients, while retaining the stability, conservation properties and implementation of this second-order method. In the following box the second-order iterative scheme is summarized.

$$i = 0 \quad (i \text{ is the iteration number})$$

Predictor phase:

$$\mathbf{u}_{n+1}^{(i)} = \tilde{\mathbf{u}}_{n+1} \quad \mathbf{v}_{n+1}^{(i)} = 0 \quad \mathbf{a}_{n+1}^{(i)} = \tilde{\mathbf{a}}_{n+1}$$

Solution phase:

$$\frac{1}{\Delta t}\mathcal{M}\Delta\mathbf{v}^{(i)} = \mathcal{F}_{n+\alpha}^{\mathrm{ext}} - \mathcal{F}^{\mathrm{int}}(\mathbf{u}_{n+\alpha}^{(i)}, \mathbf{v}_{n+\alpha}^{(i)}) - \frac{1}{\Delta t}\mathcal{M}[\mathbf{v}_{n+1}^{(i)} - \mathbf{v}_n]$$

Corrector phase:

$$\begin{aligned} \mathbf{v}_{n+1}^{(i+1)} &= \mathbf{v}_{n+1}^{(i)} + \Delta\mathbf{v} \\ \mathbf{u}_{n+1}^{(i+1)} &= \tilde{\mathbf{u}}_{n+1} + \frac{\beta\Delta t}{\gamma}\mathbf{v}_{n+1}^{(i+1)} \\ \mathbf{a}_{n+1}^{(i+1)} &= \tilde{\mathbf{a}}_{n+1} - \frac{1}{\gamma\Delta t}\mathbf{v}_{n+1}^{(i+1)} \end{aligned}$$

where the predictors are simply defined as

$$\begin{aligned} \tilde{\mathbf{u}}_{n+1} &= \mathbf{u}_n + \Delta t\left(1 - \frac{\beta}{\gamma}\right)\mathbf{v}_n + \Delta t^2\left(\frac{1}{2} - \frac{\beta}{\gamma}\right)\mathbf{a}_n \\ \tilde{\mathbf{a}}_{n+1} &= \left(1 - \frac{1}{\gamma}\right)\mathbf{a}_n - \frac{1}{\gamma\Delta t}\mathbf{v}_n \end{aligned}$$

Within this energy–momentum-conserving framework, there is no difficulty to handle a more complex constitutive behaviour, in particular to incorporate attenuation. Convergence and stability have been extensively studied by Hughes and Simo [49–51].

Numerical implementation. In all the simulations presented in this paper, the parameters of the predictor-multicorrector algorithm are $\alpha = 1/2$, $\beta = 1/2$ and $\gamma = 1$. The associated Courant number can be defined as $n_{\mathrm{C}} = \max[c\Delta t/\Delta x]$, where c is the elastic wave speed and Δx the collocation grid spacing. Since, as seen before, this Courant condition behaves like $\Delta t_{\mathrm{C}} < \mathcal{O}({n_{\mathrm{el}}}^{-1/n_d} N^{-2})$, with n_{el} the number of elements, n_d the spatial dimension and N the polynomial order, a trade-off has to be found between the h and the p discretization. Typically, when the geometry of the problem exhibits important variations and therefore imposes a high number of elements to be correctly sampled, we use a higher number of elements with a lower polynomial degree inside each element, while when the signal we want to propagate in the model has some significant energy at higher frequencies, but the geometry is smoother, we use a lower number of elements and a higher polynomial degree inside each element. In practice, in the simulations presented below, we used a polynomial approximation of order $N = 5$ or of order $N = 8$, depending on the geometry of the problem and of the frequencies involved, and empirically determined the maximum Courant number to be of the order of 0·60, which is the value that has been used in all the examples presented.

The method is shown to work accurately with a low number of grid points per minimum wavelength, corresponding to the maximal frequency $f_{\max}$ defined as the frequency above which the spectral amplitude of the source becomes less than 5 per cent of the maximum value associated with the fundamental frequency f_0. For a Ricker wavelet in time, one gets the approximate relation $f_{\max} \simeq 2{\cdot}5 f_0$. In practice, a spatial sampling of the order of 4 or 5 points per minimum wavelength has been found very accurate when working with a polynomial degree between $N = 5$ and $N = 8$, and has been used as the minimum sampling value in all the simulations presented in this article. Below this value, the solution quickly develops significant numerical oscillations during the propagation. Such an abrupt transition is characteristic of methods with minimal numerical dispersion and diffusion.

Typically, for two-dimensional simulations with a 100 000 points curvilinear grid, the memory occupation is of the order of 32 Megabytes and the CPU time, for a simulation over 2000 time steps, is of the order of 15 min on an Ultra Sparc 1 (140 MHz). For large three-dimensional simulations in a heterogeneous medium, using a 5 000 000 points curvilinear grid, the memory occupation is of the order of 1·5 Gigabyte and the CPU time, for a simulation over 2000 time steps, is of the order of 1·5 h on a CM5 128 nodes.

TWO-DIMENSIONAL NUMERICAL EXAMPLES

Three sets of examples are included here to demonstrate the numerical efficiency of the proposed procedure. Validation of the method against classical two-dimensionl analytical or numerical solutions have been extensively studied [52, 53] and will not be repeated here.

The first example is included here in order to examine the stability and the accuracy of the proposed spectral element approximation together with the behaviour of absorbing boundary conditions. Both concepts are studied by measuring the time evolution of the kinetic and potential energy in a discretized domain.

In the second example, results obtained by the spectral element method (SEM) are compared with the ones computed by more widely used numerical methods. The response of a semicircular canyon under incidence of Rayleigh waves is presented. This canonical example was first computed by Kawase [37] by means of the discrete wavenumber-boundary element method (DWNBEM) and is often regarded as a benchmark. Kawase's results have been checked recently by Ohminato and Chouet [6] using a finite difference method, and by Moczo and co-workers [54] using a hybrid method.

Finally a study case was designed to assess the performance of the method in the presence of lateral variations of topography and material properties. The ground motion is computed for an irregular layer excited by an explosive source. As for previous example, this problem has no analytical solution, so we computed the surface seismograms by means of the indirect boundary element method (IBEM).

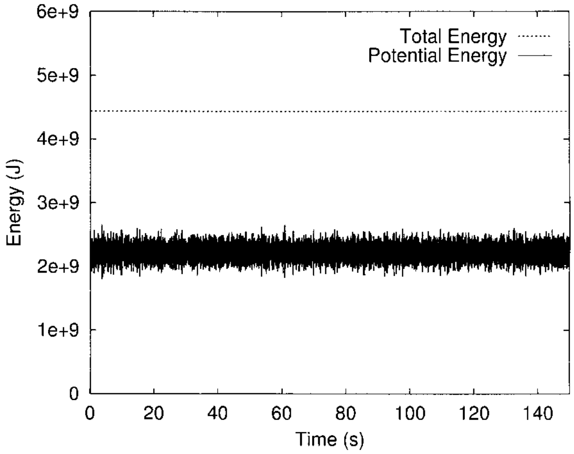

Figure 1. Long-term stability of the energy–momentum-conserving time scheme for the case of a homogeneous elastic medium, bounded by free surfaces, with a vertical force source inside the volume. The time evolution of the total and potential energy is displayed for 10^5 time steps ($\Delta t = 1{\cdot}5\,\text{ms}$). The total energy is shown to remain constant during the simulation

Energy–momentum conservation and absorbing conditions

Numerical methods tend to accumulate error as the various computations are performed. Sometimes numerical damping is implicitly introduced in the calculations, solutions degradate in amplitude and noise can prevail. In other cases amplitudes grow and also become noisy. Both situations are obviously undesirable, as we require the numerical method to be reliable and stable. First, we verify the stability of the SEM and check energy conservation inside a rectangular domain with free boundaries. In this example a force is applied at an interior point and the generated waves are allowed to propagate freely in the domain. Assuming there is no damping, waves bounce back and forth in the model. The energy provided by the applied force must be conserved within the domain. For all the elements, the elementary kinetic and potential energies are computed by means of $U_c^e = \int \frac{1}{2}\rho(\partial u_i^e/\partial t)^2\,\mathrm{d}V$ and $U_p^e = \int \frac{1}{2}\sigma_{ij}^e\varepsilon_{ij}^e\,\mathrm{d}V$, respectively. Summation on all the elements is then performed, in order to obtain the total potential and kinetic energies.

The region under study has a size of $1600 \times 1600\,\text{m}$ and is discretized using 484 spectral elements with a polynomial order of $N = 5$, the total number of points of the global grid being 12 321. The material properies of the medium are $c_\text{L} = 3200\,\text{m}\,\text{s}^{-1}$, $c_\text{T} = 1847{\cdot}5\,\text{m}\,\text{s}^{-1}$ and $\rho = 2200\,\text{kg}\,\text{m}^{-3}$. The vertical force is applied exactly at the centre of the model in $(x, z) = (800, 800)$ m and its time variation is a Ricker wavelet having a central frequency of 15 Hz. Figure 1 depicts the potential and total energies for 10^5 time steps (from 0 to 150 s), the elementary time step being $\Delta t = 1{\cdot}5\,\text{ms}$. We see a constant conversion between kinetic and potential energy and remark that, even after such a high number of time steps, the total energy remains constant. The method exhibits good stability properties.

Instead of free boundaries, we now specify absorbing conditions. According to equation (19), the necessary tractions in the variational principle are given using expression (16), which essentially corresponds to dampers. Figure 2 shows, for the same force and the same model as in previous

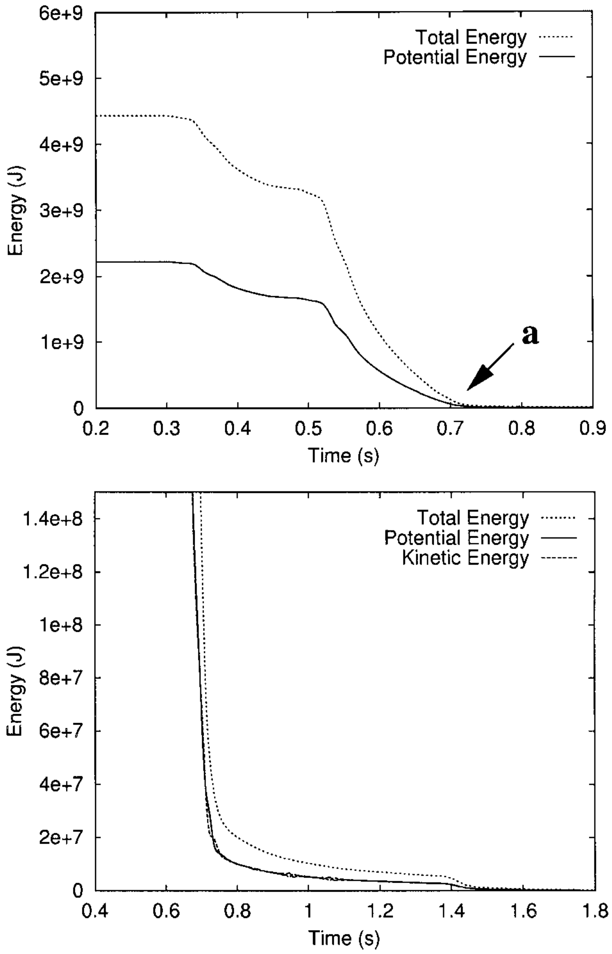

Figure 2. (Upper figure) Energy evolution for the case of a homogeneous elastic medium, limited by absorbing boundaries, when a vertical force source is applied inside the volume. The total energy decreases rapidly as the energy is radiated outside the domain. Small spurious reflections may appear for waves impinging on the boundaries at small incidence angles, due to the zeroth-order approximation used here. These spurious reflections, that keep a small fraction (less than a few percent) of the total energy in the system, are absorbed as soon as they reach a new absorbing boundary. Due to the scale, this effect is hardly visible on this figure and can only be observed when zooming on the area indicated by an arrow a. (Lower figure) Close-up of the energy residual. Potential energy converts into kinetic energy and *vice versa* around $t = 1$ s due to a parasitic corner effect. The spurious reflections are absorbed around $t = 1{\cdot}45$ s

example, the total energy. Before the waves reach the boundary, the total energy inside the domain remains constant, but once the waves start to interact with the absorbing edges, it rapidly tends to a value close to zero. The curve exhibits two steps that correspond respectively first to the absorption of the P wave (fastest wave) and second to that of the S wave (slowest wave). A small residual is visible on the close-up presented on the same figure, due to the fact that the paraxial approximation used is exact only along the normal to the boundary, and becomes less and less accurate with an increasing angle of incidence. This artificial residual is itself absorbed after having propagated through the grid, around $t = 1{\cdot}45$ s. The conversion between kinetic and potential energy around $t = 1$ s is attributed to a parasitic corner effect at a time when the different wavefronts reach the four corners of the grid.

The semicircular canyon

In the study of wave propagation in and around irregular topographies, a well-known example of Trifunac [55], namely the diffraction of a plane *SH* wave by a semicircular canyon at the surface of a half-space, it was possible to reach this classical analytical solution because of the separability of the reduced wave equation in the half-space, when cylindrical co-ordinates are used. Dealing with the propagation of *P*-*SV* waves, variables in the Navier equation in the half-space cannot be separated anymore. No analytical solution is attainable and use must be made of numerical methods. Wong [56] and Sánchez-Sesma and Campillo [38] studied the problem in the frequency domain and produced results for incident *P*, *SV* and Rayleigh waves using numerical schemes of integral type. Kawase [37] also resorted to boundary integrals, but computed the required Green's functions using the discrete wavenumber method. His results have been verified extensively [6, 54], therefore they are trustworthy. The model is characterized by $c_L = 2000\,\mathrm{m\,s^{-1}}$, $c_T = 1000\,\mathrm{m\,s^{-1}}$ (Poisson's ratio $\nu = 1/3$) and $\rho = 1000\,\mathrm{kg\,m^{-3}}$. The radius of the canyon is 1000 m. In this paper we choose to present the results for an incoming Rayleigh wave. To simulate such an excitation, the displacement, velocity and acceleration fields of the unperturbed Rayleigh wave solution are given at the initial time, and are computed from the exact solution of the problem in a half-space. Figure 3 shows two snapshots of the displacement field at time $t = 0$ and $t = 6$ s for a Rayleigh wave whose horizontal component varies as a Ricker wavelet having a fundamental frequency of 1 Hz. The computational grid of spectral elements is illustrated in the same figure. Note that the mesh is refined in the neighbourhood of the canyon. The grid is composed of 1960 elements, the polynomial order used is $N = 5$, the total number of points of the global grid being 49 596. We propagate the wavefield for 8 s (6400 time steps of $\Delta t = 1{\cdot}25$ ms each). On all the boundaries of the grid except the free surface, an absorbing condition is imposed. When the wave hits the canyon a pattern of diffracted waves is produced. In Figures 4 and 5, for horizontal and vertical components respectively, the displacement field is depicted along with Kawase's [37] plots. The 71 receivers are located exactly at the free surface between $x = -3$ and $x = 3$ km. The agreement is excellent and our results are free of numerical artefacts. The stability of the generated surface wave is verified since it propagates correctly with no dispersion and with the appropriate velocity. Several comparisons were done with other computations by Kawase for incident *P* or *SV* waves. In all cases (not presented here) the agreement was very good. It is instructive to examine the spectral ratio for the displacement with respect to the unperturbed horizontal displacement of the surface wave. In Figure 6 we present the normalized motion, at the central Ricker frequency, along the line of receivers located at the surface. A large amplification on the left side of the canyon and a great reduction at the opposite rim are clearly observed. The presence of the canyon creates a shadow zone, and this is the reason why, in some cases of engineering interest, trenches are used as devices for vibration insulation.

An irregular layer

To study the behaviour of the method in the presence of lateral irregularity and spatial variation of material properties, the ground motion is computed for an irregular layer in the case of an explosive source located close to the bottom of the layer. As for previous example, this problem has

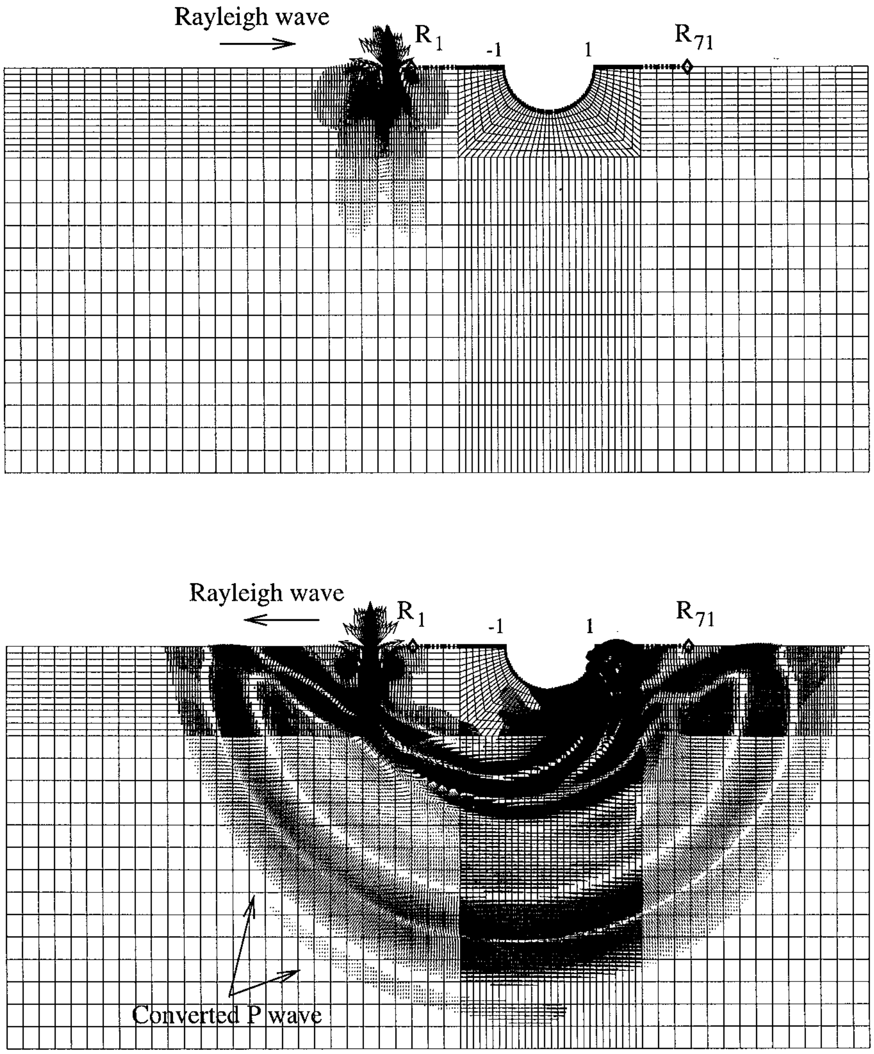

Figure 3. Snapshots illustrating the displacement field as well as the spectral element grid at the initial time (upper figure) and at time $t = 6$ s (lower figure) for the problem of a semicircular canyon excited by a Rayleigh wave. On all the boundaries of the grid except the free surface, an absorbing condition is imposed. We clearly see a P wave, generated by conversion at the canyon profile, a reflected Rayleigh wave, as well as numerous weak phases propagating inside the canyon. Each figure is normalized independently with respect to the maximum of the norm of the displacement vector at the corresponding time

no analytical solution, so we computed the surface seismograms by means of the indirect boundary element method (IBEM). In the IBEM, the homogeneity of the regions involved is assumed. This allows us to make use of the well-known exact Green's function for the full elastic space [38, 57]. The application of the IBEM in the context of irregular layers has been described elsewhere [39]. The spectral element computational grid is depicted in Figure 7, together with the source and receivers locations. The grid is composed of 874 elements and a polynomial order of $N = 5$ has

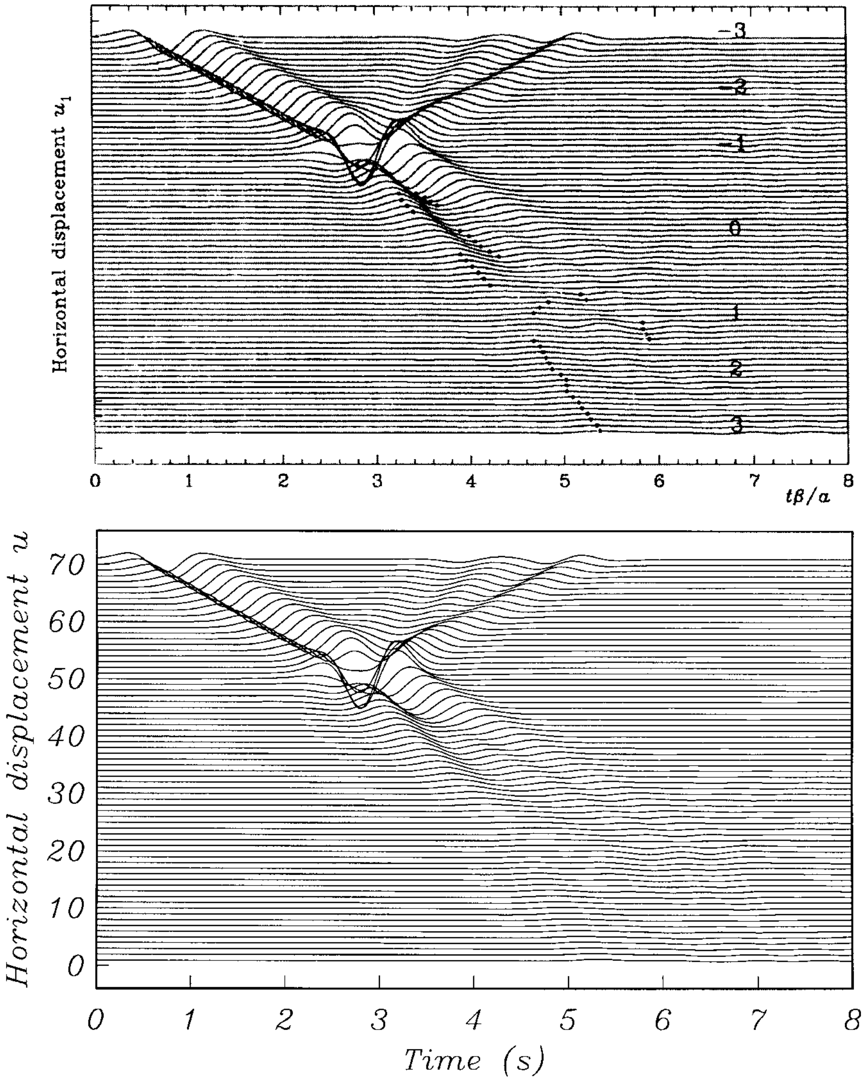

Figure 4. Horizontal displacement synthetic seismograms calculated along the free surface of the semicircular canyon of Figure 3 excited by a Rayleigh wave. The upper figure is a copy of the results published by Kawase (1988), Figure 14(a), the lower figure represents our results drawn at the same scale. The overall agreement is very good apart from some weak parasitic oscillations that appear in the DWNM calculations after $t \simeq 6$ s

been used, leading to a global grid made of 22 176 points. The time step used is $\Delta t = 6{\cdot}25$ ms, and the wavefield is propagated for 25 s (4000 time steps). The depth of the interface varies from 1 to 1·5 km, its geometry being described in kilometres by the function $z = 1 + 0{\cdot}5\cos^2(\pi x/2)$ for $|x| \leqslant 1$, therefore the width of the irregularity is 2 km. The material properties of the media are: $c_{T_{\mathrm{hs}}} = 1500\,\mathrm{m\,s^{-1}}$ and $c_{T_{\mathrm{lay}}} = 500\,\mathrm{m\,s^{-1}}$ (in the half-space and in the layer respectively), with a Poisson's ratio of $\nu = 1/3$ in both cases; the densities are $\rho_{\mathrm{hs}} = 2000\,\mathrm{kg\,m^{-3}}$ and $\rho_{\mathrm{lay}} = 1000\,\mathrm{kg\,m^{-3}}$.

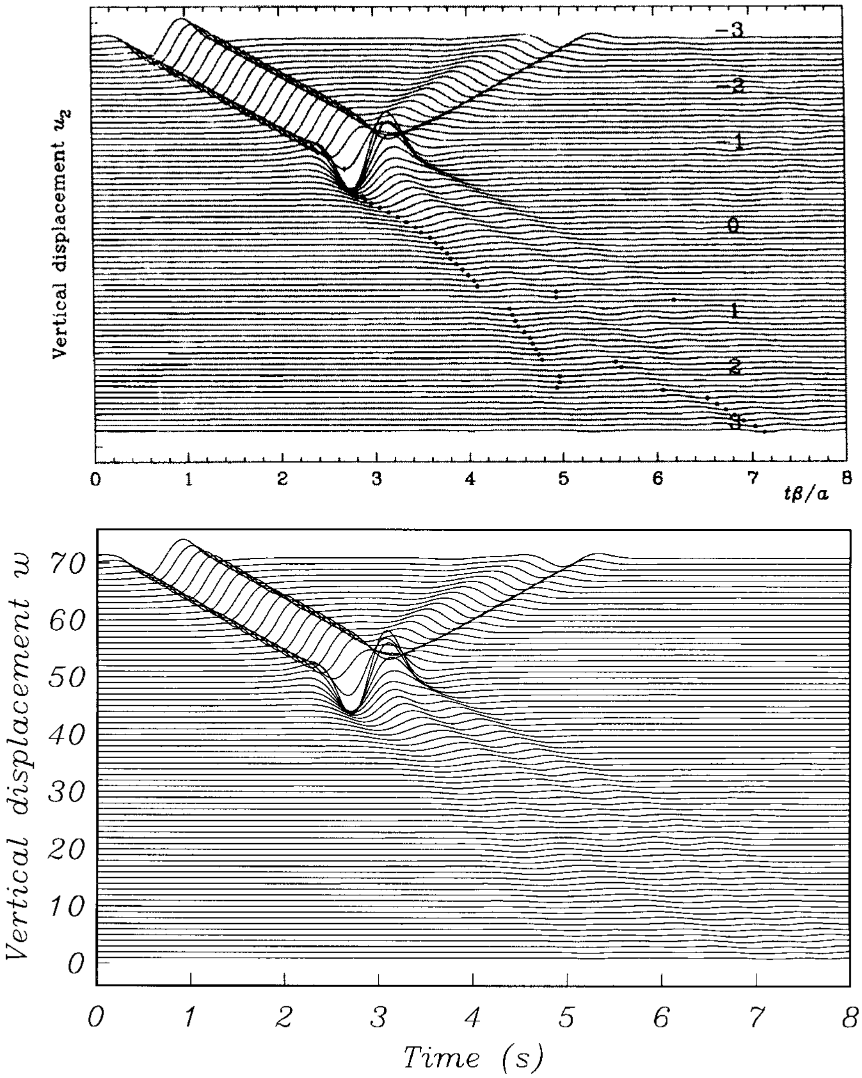

Figure 5. Vertical displacement synthetic seismograms calculated along the free surface of the semicircular canyon of Figure 3 excited by a Rayleigh wave. The upper figure is a copy of the results published by Kawase [37] (Figure 14b), the lower figure represents our results drawn at the same scale. The overall agreement is again very good, with the same weak artefacts in the DWNM calculations, as in Figure 4

On all the boundaries of the grid except the free surface, an absorbing condition is imposed. The source, located at 3000 m in depth and 1000 m away from the topography symmetry axis, is assumed to be isotropic (explosion) with a time history given by a Ricker wavelet with a central frequency of 0·75 Hz. Synthetic seismograms are given for 51 receivers located along the flat free surface between $x = -2$ and $x = 2$ km; the spatial interval between stations is 80 m.

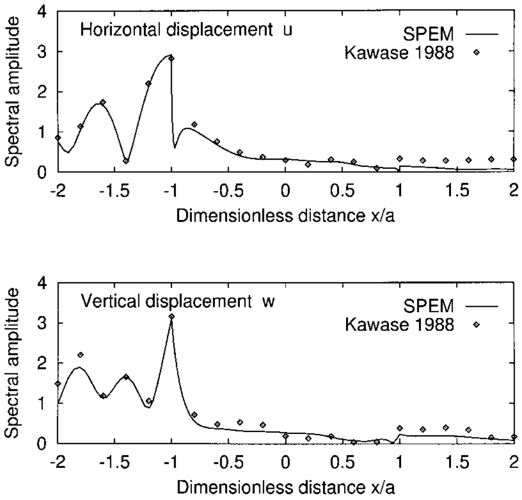

Figure 6. Spectral amplitude, at the Ricker central frequency, calculated along the free surface of the semicircular canyon of Figure 3 excited by a Rayleigh wave. Our solution (solid line) is very close to the results of Kawase (points). Near the right edge of the canyon, Kawase's results seem to present a signal excess (the spectral amplitude seems to be slightly too high) that is probably due to the weak oscillations observed in Figures 4 and 5

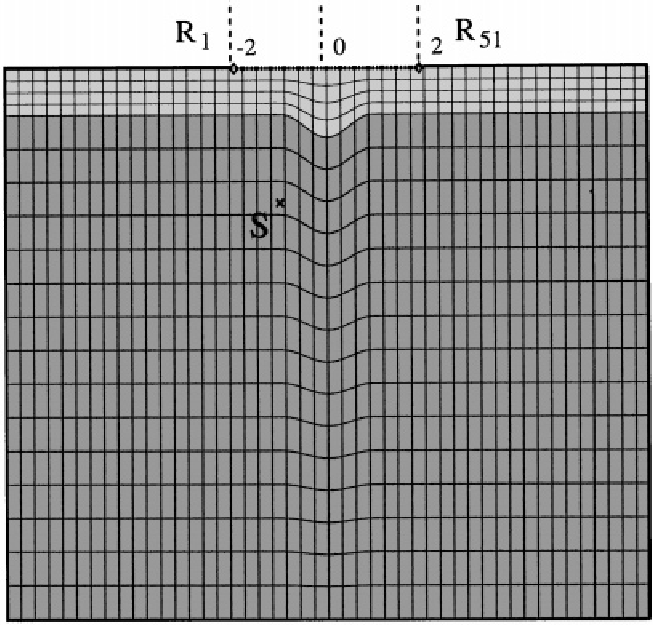

Figure 7. Model and grid used to compute the seismic response of an irregular layer with a flat free surface. The excitation is provided by a linear explosive source located 3000 m deep in the model, and 1000 m away from the symmetry axis of the topography of the interface. On all the boundaries of the grid except the free surface, an absorbing condition is implemented

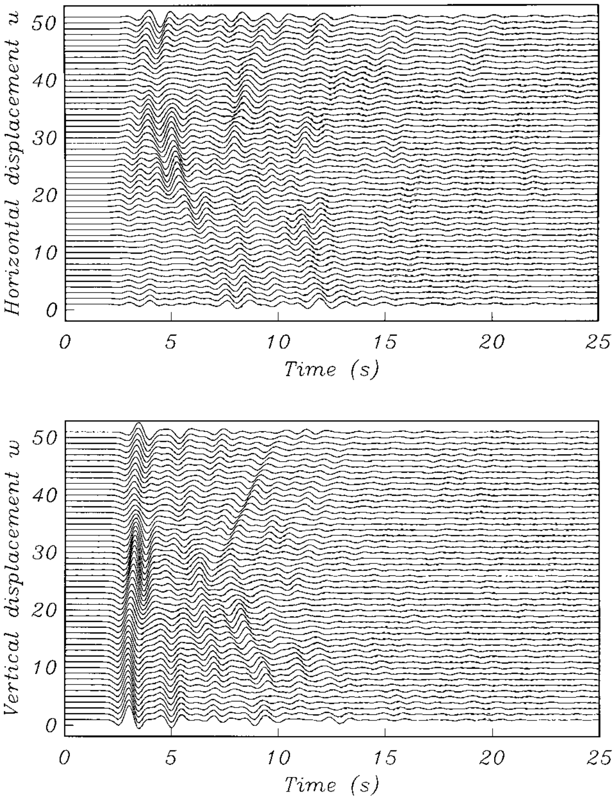

Figure 8. Synthetic seismograms along the flat free surface of the irregular layer of Figure 7 excited by a low frequency explosive source located in the underlying half-space. Results obtained with SEM (solid line) and IBEM (dashed line) are superimposed. The overall agreement is very good during the first 10–12 s, then small differences of weak amplitude appear

The waveforms obtained with both IBEM and SEM are superimposed and are plotted with solid and dashed lines, respectively, in Figure 8. The agreement is very good and, given the fact that the solutions are obtained with completely different methods, fully validates both the SEM and the IBEM. Some small differences can be seen in the later parts of the seismograms. Understanding the origin of these differences will require additional work. In any case, both methods are reliable.

When we analyse the ground motion, we notice that the last stations record a *P* first arrival, followed by a *P* wave multiple, generated at the plane interface between the layer and the half-space. Then, surface waves arrive. Apparently, no multiples can be seen at the centre of the array. At the right side of the irregularity, a shadow zone exists, just as in the previous example. Displacements near the right edge of the bump are relatively small, when compared to the other traces. As distance from this protected area increases, the first arrival and its multiple are reconstructed. The maximum displacement is recorded inside the valley, where constructive interferences occur. On the other hand, the duration of the vibrations is longer at the extreme stations. *P*-*SV* reflection energy rapidly decays, while surface waves propagate further.

THREE-DIMENSIONAL NUMERICAL EXAMPLES

The three-dimensional response of a hill

In previous sections, we studied the stability and the accuracy of computations using the SEM in two-dimensional cases. Now we describe the application of this technique to study a three-dimensional smooth topographical profile. Recent studies [58, 59] have pointed out the important effects of a small three-dimensional hill structure and their implications for strong ground motion. The mesh for this model is depicted in Figure 9. The topography is described by a bi-variate Gaussian function (the maximum height is 180 m, the standard deviations along the two perpendicular directions are 250 and 125 m respectively) and its horizontal projection is elliptic. The material properties of the medium are $c_L = 3200\,\mathrm{m\,s^{-1}}$, $c_T = 1847{\cdot}5\,\mathrm{m\,s^{-1}}$ and $\rho = 2200\,\mathrm{kg\,m^{-3}}$. The size of the model is $2080 \times 2080 \times 1050$ m and the height of the hill is 180 m. The mesh is composed of $26 \times 26 \times 14$ elements, with a polynomial order of $N = 8$ used in each direction, leading to a total number of collocation points of 4 935 953. On the vertical boundaries of the grid, periodic conditions are imposed, meaning that the model is infinitely repeated identically along the two horizontal directions. The total duration of the simulation is 0·8 s, with a time step of $\Delta t = 0{\cdot}5$ ms. Such a duration is short, but intrinsically limited by the arrival time of the parastic waves induced by the use of periodic boundary conditions, due to the finite size of the model.

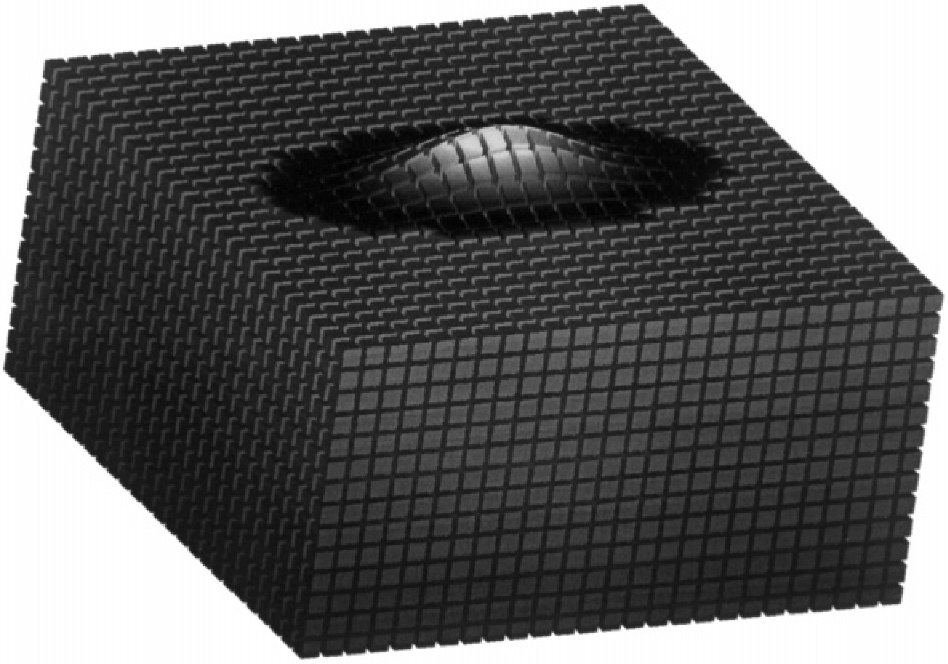

Figure 9. Three-dimensional model: a 3-D Gaussian shape topography is considered in the case of a homogeneous elastic half-space. The size of the model is $2080 \times 2080 \times 1050$ m. The height of the hill is 180 m. The mesh is composed of $26 \times 26 \times 14$ elements, with a polynomial order of $N = 8$ used in each direction. The total number of collocation points is 4 935 953. On vertical boundaries, periodic conditions are imposed

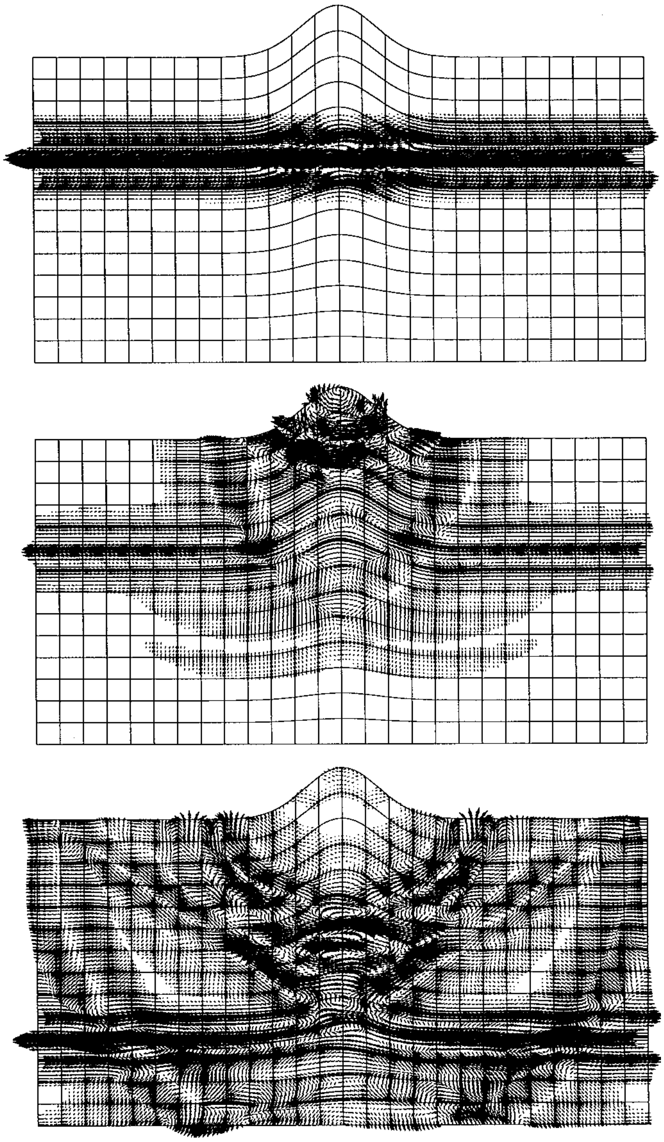

Figure 10. Snapshots at time $t = 0$ (top), 0·4 (middle) and 0·6 s (bottom) for the model of Figure 9 excited by an S wave polarized along the direction of the small axis of the topography. The vertical cut is done along the direction of polarization. The displacement vector is projected onto the cut plane. The topography generates an important P wave as well as a Rayleigh wave that propagates down the slope

The incoming vertical plane shear wave is polarized along the small axis, and the time variation is given by a Ricker pulse having a central frequency of 10·26 Hz. Note that the incident wavelength is 180 m, precisely the height of the topography.

Figure 10 illustrates three snapshots of particle displacement. They correspond to a vertical cut along the minor axis at different times ($t = 0, 0{\cdot}4$ and 0·6 s). In the upper plot the incident

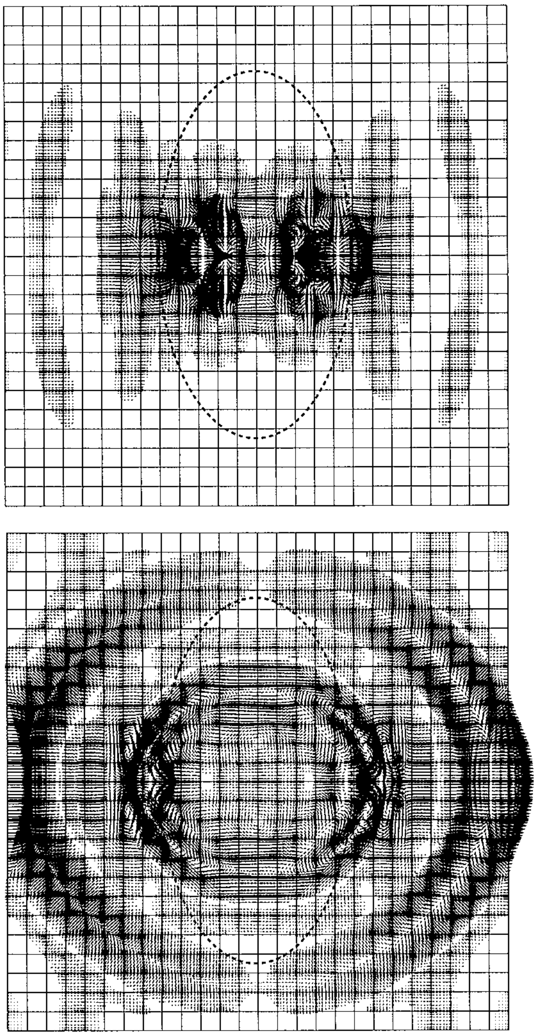

Figure 11. Displacement field at the surface, for the model of Figure 9, projected onto an horizontal plane (top view). The two snapshots are drawn at time $t = 0{\cdot}4$ (top) and $0{\cdot}6\,\mathrm{s}$ (bottom) as in Figure 10. The elliptic base of the hill is represented by a dashed line. Clearly-visible Rayleigh and diffracted waves preferentially propagate along the small axis direction

shear wave has not reached the free surface yet, the apparently irregular structure of the plot is a visual effect due to the grid geometry (having a non-uniform grid spacing inside each element). On the other plots, the direct wave reaches the free surface where it is reflected downwards, and significant elastic wave diffraction appears. On the second plot we can see the main reflected wave propagating towards the lower boundary, and the other waves generated by the presence of the topography. One can recognize the P wave that travels ahead. One can remark the focusing of various diffracted waves inside the hill. This phenomenon gives rise to a significant amplification of the ground motion. At this time ($t = 0{\cdot}4\,\mathrm{s}$) the maximum horizontal displacement appears to be at the inner base of the irregularity. On the other hand, large vertical displacements can also

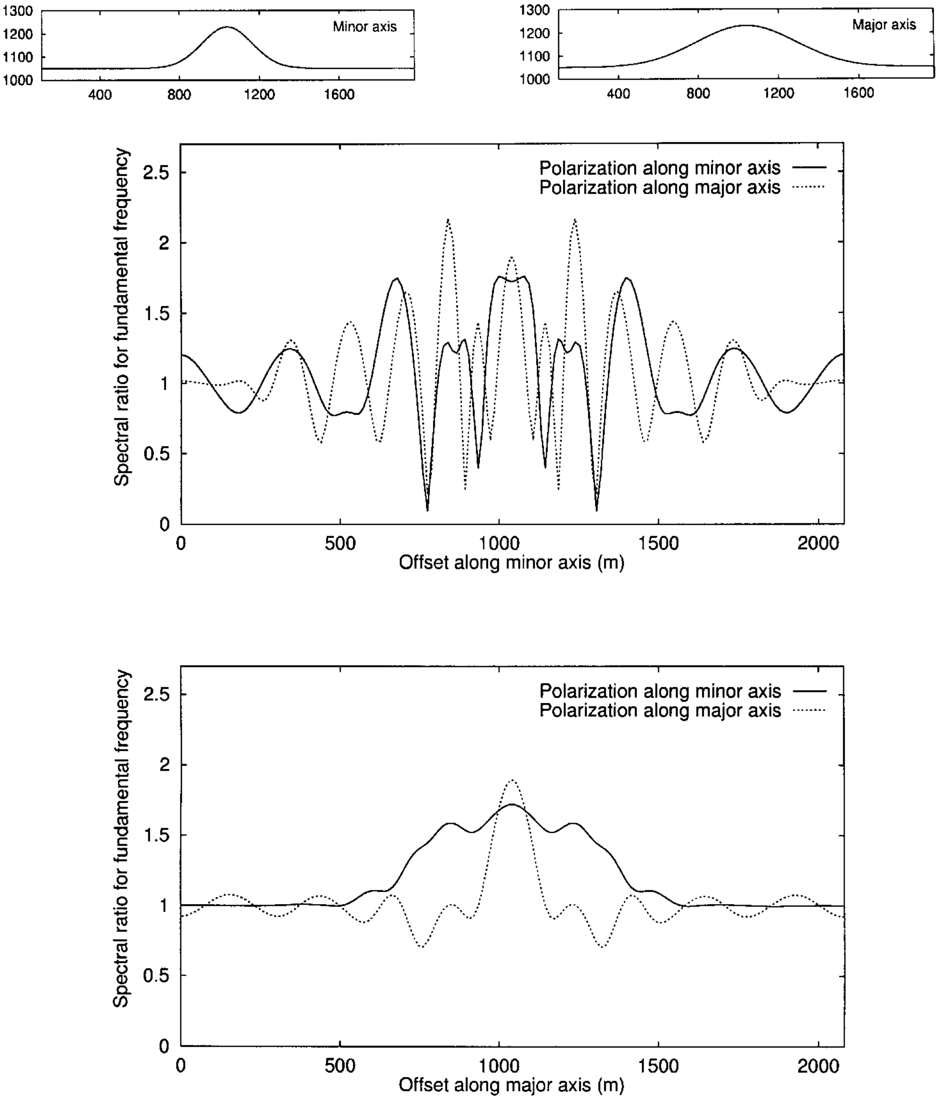

Figure 12. Transfer function at the Ricker fundamental frequency along two lines of receivers located at the surface of the model. Upper figure: response recorded along the minor axis. Lower figure: response recorded along the major axis. The transfer function is computed as the ratio between the spectral amplitude of the component of the displacement vector along the direction of polarization of the plane wave source and the spectral amplitude of that incident wave. In each figure, two different sources are considered, namely a vertically incident S wave polarized either along the minor or along the major axis. A strong variation of the recorded amplification pattern can be observed, underlining the need for 3-D simulation of site amplification even in the case of rather simple models

be seen on the topographical profile. We interpret these ripples as the birth of Rayleigh waves. In fact, the third snapshot clearly shows the familiar displacement pattern of these waves, with their typical elliptical polarization. Note that the hole in the reflected wave front is being filled by the local diffraction. The snapshots depict many other waves produced in this process. We can recognize in particular several phases of shear waves and the *SP* head waves diffracted by the interaction of the *P* wave with the free surface.

Two snapshots of the surface motion, normalized independently with respect to the maximum of the norm of the displacement vector at the surface, are given in Figure 11 at the same time as the last two snapshots of Figure 10 ($t = 0{\cdot}4$ and $0{\cdot}6$ s). They show from another perspective (top view) the weak emission of a diffracted *P* wave at the surface and the significant generation of Rayleigh waves, particularly along the minor axis of the topography. Ground motion along this direction is remarkably stronger than for the other direction. This clearly demonstrates the importance of three-dimensional effects in non-symmetric stuctures and confirms the existence of preferred directional resonances [60, 61]. On the second snapshot, we also clearly see a numerical parasitic effect (artificial waves coming from the boundaries of the model) that are due to the periodic boundary conditions used on the vertical edges of the model.

The difference between ground motions along two perpendicular seismic lines is confirmed in Figure 12, where displacement transfer functions (computed at the Ricker central frequency) are plotted along these lines. The transfer function is computed as the ratio between the spectral amplitude of the component of the displacement vector recorded along the direction of polarization of the source, and the spectral amplitude of the plane wave. Two different sources are considered: a *S* wave polarized along the minor axis of the topography, and a *S* wave polarized along the major axis. In both cases, the transfer function has been computed for the component of the displacement along the same axis as the direction of polarization of the incident wave. We do not observe any significant difference in the maximum amplification level. However, the three-dimensonal effect is revealed by the completely dissimilar movement pattern illustrated in both figures. Along the minor axis, the response shows large oscillations that suggest important differential motion. We know that this is due to a modulation of the signal by Rayleigh waves that travel downwards along the slope, preferentially along the minor axis of the topography as seen before. On the other direction, the effects on ground motion are much smaller. The highest perturbation is restricted to a narrow spatial zone around the summital area.

CONCLUSIONS

A new tool to simulate elastic wave propagation in arbitrary models has been presented. The formulation of this spectral element method (SEM) has been detailed. The technique is suitable to an efficient parallel implementation and has a low computational cost. We illustrated the method with two simple cases in which the stability and consistency of the approach have been underlined. More realistic models were then considered. The two-dimensional examples (a semicircular canyon and an irregularly stratified medium) offered the opportunity to validate the SEM by comparing our synthetic seismograms to those obtained with very different methods. The agreement between the results has been found to be very good. Finally, a three-dimensional model has been discussed. The different tests presented underline the potentialities of the SEM. This technique appears to fulfill the requirements (low cost and high accuracy) of modern computational seismology. It seems to be a powerful tool for efficient prediction and interpretation of site effects in seismic ground motion.

ACKNOWLEDGEMENTS

The authors would like to thank R. Madariaga for his constructive and keen critical remarks. H. Kawase kindly provided us with original reprints of his paper on the semicircular canyon. This work has been partially supported by DGAPA-UNAM, Mexico, under Grant IN108295.

Computations were done on the CM5 128 nodes of the French Centre National de Calcul Parallèle en Sciences de la Terre (CNCPST).

REFERENCES

1. Virieux J. *P-SV* wave propagation in heterogeneous media: velocity-stress finite-difference method. *Geophysics* 1986; **51**:889–901.
2. Levander AR. Fourth-order finite-difference *P-SV* seismograms. *Geophysics* 1988; **53**:1425–1436.
3. Dablain MA. The application of high-order differencing to the scalar wave equation. *Geophysics* 1986; **51**(1):54–66.
4. Bayliss A, Jordan KE, Lemesurier BJ, Turkel E. A fourth-order accurate finite-difference scheme for the computation of elastic waves. *Bulletin of the Seismological Society of America* 1986; **76**:1115–1132.
5. Jih RS, McLaughlin KL, Der ZA. Free-boundary conditions of arbitrary polygonal topography in a two-dimensional explicit elastic finite-difference scheme. *Geophysics* 1988; **53**:1045–1055.
6. Ohminato T, Chouet BA. A free-surface boundary condition for including 3D topography in the finite difference method. *Bulletin of the Seismological Society of America* 1997; **87**:494–515.
7. Frankel A. Three-dimensional simulations of ground motions in the San Bernardino valley, California, for hypothetical earthquakes on the San Andreas fault. *Bulletin of the Seismological Society of America* 1993; **83**;1020–1041.
8. Olsen KB, Archuleta RJ. 3-D simulation of earthquakes on the Los Angeles fault system. *Bulletin of the Seismological Society of America* 1996; **86**(3):575–596.
9. Lysmer J, Drake LA. A finite element method for seismology. In *Methods in Computational Physics*, vol. 11. Academic Press: New York, 1972.
10. Marfurt KJ. Accuracy of finite-difference and finite-element modeling of the scalar wave equations. *Geophysics* 1984; **49**:533–549.
11. Hulbert GM, Hughes TJR. Space-time finite element methods for second-order hyperbolic equations. *Computer Methods in Applied Mechanics and Engineering* 1990; **84**:327–348.
12. Richter GR. An explicit finite element method for the wave equation. *Applied Numerical Mathematics* 1994; **16**:65–80.
13. Thompson LL, Pinsky P. A space-time finite element method for structural acoustics in infinite domains. Part 1: Formulation, stability and convergence. *Computer Methods in Applied Mechanics and Engineering* 1996; **132**:195–227.
14. Manolis G, Beskos DE. *Boundary Element Methods in Elastodynamics*. Unwin Hyman: London, 1988.
15. Bonnet M. *Équations intégrales et éléments de frontière*. CNRS Éditions: Eyrolles, Paris, 1995.
16. Sánchez-Sesma FJ, Rosenblueth E. Ground motion at canyons of arbitrary shape under incident *SH* waves. *Earthquake Engineering and Structural Dynamics* 1979; **7**:441–450.
17. Sánchez-Sesma FJ, Ramos-Martinez J, Campillo M. An indirect boundary element method applied to simulate the seismic response of alluvial valleys for incident *P*, *SV* and Rayleigh waves. *Earthquake Engineering and Structural Dynamics* 1993; **22**:279–295.
18. Aki K, Larner KL, Surface motion of a layered medium having an irregular interface, due to incident plane *SH* waves. *Journal of Geophysical Research* 1970; **75**:933–954.
19. Bouchon M. Discrete wavenumber representation of elastic wave fields in three space dimensions. *Journal of Geophysical Research* 1979; **84**:3609–3614.
20. Géli L, Bard PY, Julien B. The effect of topography on earthquake ground motion: a review and new results. *Bulletin of the Seismological Society of America* 1988; **78**:42–63.
21. Bouchon M, Aki K. Discrete wavenumber representation of seismic-source wave fields. *Bulletin of the Seismological Society of America* 1977; **67**:259–277.
22. Kawase H, Aki K. A study on the response of a soft sedimentary basin for incident *S*, *P* and Rayleigh waves, with special reference to the long duration observed in Mexico City. *Bulletin of the Seismological Society of America* 1989; **79**:1361–1382.
23. Gazdag J. Modeling of the acoustic wave equation with transform methods. *Geophysics* 1981; **46**:854–859.
24. Kosloff D, Baysal E. Forward modeling by the Fourier method. *Geophysics* 1982; **47**:1402–1412.
25. Fornberg B. The pseudospectral method: accurate representation of interfaces in elastic wave calculations. *Geophysics* 1988; **53**:625–637.
26. Kosloff D, Kessler D, Filho AQ, Tessmer E, Behle A, Strahilevitz R. Solution of the equations of dynamics elasticity by a Chebyshev spectral method. *Geophysics* 1990; **55**:748–754.
27. Carcione JM, Wang PJ. A Chebyshev collocation method for the wave equation in generalized coordinates. *Computers and Fluid Dynamics Journal* 1993; **2**:269–290.
28. Carcione JM. Domain decomposition for wave propagation problems. *Journal of Scientific Computing* 1991; **6**(4): 453–472.
29. Patera AT. A spectral element method for fluid dynamics: laminar flow in a channel expansion. *Journal of Computational Physics* 1984; **54**:468–488.
30. Maday Y, Patera AT. Spectral element methods for the incompressible Navier–Stokes equations. In *State of the Art Survey in Computational Mechanics*, Noor AK, Oden JT (eds). 1989:71–143.

31. Babuška I, Szabó BA, Katz IN. The p version of the finite element method. *SIAM Journal on Numerical Analysis* 1981; **18**:512–545.
32. Priolo E, Carcione JM, Seriani G, Numerical simulation of interface waves by high-order spectral modeling techniques. *Journal of the Acoustical Society of America* 1994; **95**(2):681–693.
33. Faccioli E, Maggio F, Quarteroni A, Tagliani A. Spectral-domain decomposition methods for the solution of acoustic and elastic wave equations. *Geophysics* 1996; **61**(4):1160–1174.
34. Faccioli E, Maggio F, Paolucci R, Quarteroni A. 2D and 3D elastic wave propagation by a pseudo-spectral domain decomposition method. *Journal of Seismology* 1997; **1**:237–251.
35. Orszag SA. Spectral methods for problems in complex geometries. *Journal of Computational Physics* 1980; **37**:70–92.
36. Fischer P. Analysis and application of a parallel spectral element method for the solution of the Navier–Stokes equations. *Computer Methods in Applied Mechanics and Engineering* 1990; **80**:483–491.
37. Kawase H. Time-domain response of a semi-circular canyon for incident *SV*, *P* and Rayleigh waves calculated by the discrete wavenumber boundary element method. *Bulletin of the Seismological Society of America* 1988; **78**:1415–1437.
38. Sánchez-Sesma FJ, Campillo M. Diffraction of *P*, *SV* and Rayleigh waves by topographic features: a boundary integral formulation. *Bulletin of the Seismological Society of America* 1991; **81**:2234–2253.
39. Vai R, Castillo-Covarrubias JM, Sánchez-Sesma FJ, Komatitsch D, Vilotte JP. Elastic wave propagation in an irregularly layered medium. *Soil Dynamics and Earthquake Engineering* 1999; **18**:11–18.
40. Madariaga R. Earthquake source theory: a review. In *Earthquakes*, *Observation Theory and Interpretation*, Kanamori H, Boschi E. (eds). North-Holland: Amsterdam, 1983, The Enrico Fermi Summer School of Physics, 55th course.
41. Givoli D. Non-reflecting boundary conditions: review article. *Journal of Computational Physics* 1991; **94**:1–29.
42. Givoli D, Keller JB. Non-reflecting boundary conditions for elastic waves. *Wave motion* 1990; **12**:261–279.
43. Thompson LL, Pinsky P. A space-time finite element method for structural acoustics in infinite domains. Part 2: Exact time-dependent non-reflecting boundary conditions. *Computer Methods in Applied Mechanics and Engineering* 1996; **132**:229–258.
44. Thompson LL. Design and analysis of space-time and Galerkin-least-squares finite element methods for fluid structure interactions in exterior domains. *Ph.D. Thesis*, Stanford University, California, 1994.
45. Clayton R, Engquist B. Absorbing boundary conditions for acoustic and elastic wave equations. *Bulletin of the Seismological Society of America* 1977; **67**:1529–1540.
46. Stacey R. Improved transparent boundary formulations for the elastic wave equation. *Bulletin of the Seismological Society of America* 1988; **78**(6):2089–2097.
47. Maday Y, Rønquist EM. Optimal error analysis of spectral methods with emphasis on non-constant coefficients and deformed geometries. *Computer Methods in Applied Mechanics and Engineering* 1990; **80**:91–115.
48. Tordjman N. Éléments finis d'ordre élevé avec condensation de masse pour l'équation des ondes. *Ph.D. Thesis*, Université Paris IX Dauphine, Paris, 1995.
49. Simo JC, Tarnow N, Wong KK. Exact energy-momentum conserving algorithms and symplectic schemes for nonlinear dynamics. *Computer Methods in Applied Mechanics and Engineering* 1992; **100**:63–116.
50. Tarnow N, Simo JC. How to render second order accurate time-stepping algorithms fourth order accurate while retaining the stability and conservation properties. *Computer Methods in Applied Mechanics and Engineering* 1994; **115**: 233–252.
51. Hughes TJR. *The Finite Element Method, Linear Static and Dynamic Finite Element Analysis*. Prentice-Hall International: Englewood Cliffs, NJ, 1987.
52. Komatitsch D. Méthodes spectrales et éléments spectraux pour l'équation de l'élastodynamique 2D et 3D en milieu hétérogène, *Ph.D. Thesis*, Institut de Physique du Globe de Paris, Paris, 1997.
53. Komatitsch D, Vilotte JP. The spectral element method: an efficient tool to simulate the seismic response of 2D and 3D geological structures. *Bulletin of the Seismological Society of America* 1998; **88**:368–392.
54. Moczo P, Bystrický E, Kristek J, Carcione JM, Bouchon M. Hybrid modeling of *P-SV* seismic motion at inhomogeneous viscoelastic topographic structures. *Bulletin of the Seismological Society of America* 1997; **87**:1305–1323.
55. Trifunac MD. Scattering of plane *SH* waves by a semi-cylindrical canyon. *Earthquake Engineering and Structural Dynamics* 1973; **1**:267–281.
56. Wong HL. Effect of surface topography on the diffraction of *P*, *SV* and Rayleigh waves. *Bulletin of the Seismological Society of America* 1982; **72**:1167–1183.
57. Pedersen HA, Sánchez-Sesma FJ, Campillo M. Three-dimensional scattering by two-dimensional topographies. *Bulletin of the Seismological Society of America* 1994; **84**:1169–1183.
58. Bouchon M, Schultz CA, Töksoz MN. Effect of three-dimensional topography on seismic motion. *Journal of Geophysical Research* 1996; **101**:5835–5846.
59. Bouchon M, Barker JS. Seismic response of a hill: the example of Tarzana, California. *Bulletin of the Seismological Society of America* 1996; **86**(1A):66–72.
60. Bonamassa O, Vidale JE. Directional site resonances observed from aftershocks of the 18th October 1989 Loma Prieta earthquake. *Bulletin of the Seismological Society of America* 1991; **81**:1945–1957.
61. Spudich P, Hellweg M, Lee WHK. Directional topographic site response at Tarzana observed in aftershocks of the 1994 Northridge, California, earthquake: implications for mainshock motions. *Bulletin of the Seismological Society of America* 1996; **86**(1B):S193–S208.